DOI: 10.1002/ ((please add manuscript number))

**Article type: Communication**

# Title: Unlocking the Single-Domain Epitaxy of Halide Perovskites

*Dr. Lili Wang[†], Pei Chen[†], Dr. Non Thongprong, Margaret Young, Padmanaban S. Kuttipillai, Chuanpeng Jiang, Prof. Pengpeng Zhang, Dr. Kai Sun, Prof. Phillip M. Duxbury, Prof. Richard R. Lunt[*]*

Dr. Lili Wang, Pei Chen, Margaret Young, Padmanaban S. Kuttipillai, Prof. Richard R. Lunt
Department of Chemical Engineering and Materials Science, Michigan State University, East Lansing, MI 48824 USA

Dr. Non Thongprong, Chuanpeng Jiang, Prof. Pengpeng Zhang, Prof. Phillip M. Duxbury, Prof. Richard R. Lunt
Department of Physics and Astronomy, Michigan State University
East Lansing, MI 48824 USA

Dr. Kai Sun

Department of Material Science and Engineering, University of Michigan

Ann Arbor, MI 48109 USA

[†]These authors contributed equally to this work.

*Corresponding author. Email: rlunt@msu.edu

Keywords: Halide Perovskite; Epitaxy; 2D Quantum Well; Single-Domain; Vapor-Deposition

The growth of epitaxial semiconductors and oxides has long since revolutionized the electronics and optics fields, and continues to be exploited to uncover new physics stemming from quantum interactions. While the recent emergence of halide perovskites offer exciting new opportunities for a range of thin-film electronics, the principles of epitaxy have yet to be applied to this new class of materials and the full potential of these materials is still not yet known. In this work we demonstrate single-domain inorganic halide perovskite epitaxy. This is enabled by room-temperature reactive vapor

phase deposition onto single crystal metal halide substrates with congruent ionic interactions. For the archetypical halide perovskite, $CsSnBr_3$, we uncover two epitaxial phases, a cubic phase and tetragonal phase, which emerge via stoichiometry control that are both stabilized with vastly differing lattice constants and accommodated via epitaxial rotation. We exploit this epitaxial growth to demonstrate multilayer 2D quantum wells of a halide-perovskite system. This work ultimately unlocks new routes to push halide perovskites to their full potential.

## 1. Introduction

Hybrid halide perovskites have attracted tremendous attention as an exceptional new class of semiconductors for solar harvesting,[1] light emission,[2] lasing,[3] quantum dots,[4] water splitting[5] and thin film electronics.[6] Although efficiencies of solar cells based on hybrid organic-inorganic lead halide perovskites have exceeded 22%,[7] the toxicity of lead devices and lead manufacturing[8, 9] combined with the instability of organic components[9] have been two key barriers to widespread application. Tin-based inorganic halide perovskites, such as $CsSnX_3$ (X = Cl, Br, and I), have been considered promising substitutes for their lead analogues since Sn is over 100 times less toxic than Pb and Cs has similar toxicity to Na or K. However, current research on photovoltaic and electronic applications of $CsSnBr_3$ and $CsSnI_3$ has, to date, been less encouraging, with solar cell efficiencies of < 5% for solution-processed thin film devices[10] that are likely limited by the low degree of crystalline ordering.[11] Indeed, structural ordering has been linked in traditional semiconductors to a) carrier transport, where mobilities increase from amorphous-Si (1 $cm^2$/V-s)[12] to single crystalline Si (1,400 $cm^2$/V-s),[13] b) recombination rates, where unpassivated grain boundaries act as quenching sites for charge carriers and excited states and c) quantum confinement, which can make even Si an excellent NIR emitter with luminescent efficiency > 60%.[14] These factors, among others, have motivated the recent interest in halide perovskite single crystal growth.[15] Thus, one of the main challenges for enhancing the properties of halide perovskites for high end optoelectronic applications is to obtain epitaxial crystalline films that can also be integrated into heteroepitaxial and quantum well

structures. The epitaxial growth is a key step towards realizing 2-dimensional (2D) electron gasses,[16] interface superconductivity,[17] ultra-high mobility strained transistors,[18] magnetoelectric multiferroics,[19] and the observation of fractional quantum hall effects.[20] As shown in previous research on oxide perovskites, numerous phases can be derived from the perovskite structure with even minor changes in the elemental compositions. For example, by removing one-sixth of the oxygen atoms, phase transitions can occur from perovskite to brownmillerite structures.[21] Therefore, it is key to gain precise control over the crystal phase, crystalline order, orientation, and interfaces for the optimization of halide perovskite based optoelectronics.

While there has been significant research into the epitaxial growth of oxide perovskites,[22, 23] single-domain epitaxy has yet to be explored for halide perovskites. This has likely been hindered in large part due to a number of challenges associated with the epitaxial growth of perovskites on dissimilar single crystal substrates including matching of lattice constants, lattice symmetry, coordination, wettability, thermal expansion differences, and bonding character (ionic versus covalent)[24]. There have been only a few reports of even *metal halide salt* epitaxy[25], and only several recent studies of incommensurate Van der Waals epitaxy (or quasiepitaxy) of halide perovskite micro-sheets[26], nanorods[27], nanowires[28] and nanocrystals[29] that are accompanied with a high degree of rotational disorder. To help understand the full potential of these exciting materials, we report a low cost vapor phase route to the epitaxial growth of single-domain inorganic halide perovskites that is enabled by lattice matching on single crystal alkali halide salt substrates and further enhanced by tuned pseudomorphic interlayers of alloyed alkali halide salts. We use this as a platform to demonstrate precise control in the fabrication of 2D quantum well multilayer

structures that could translate opportunities from other emergent phenomena[17, 23] to halide perovskites.

Metal halide salts are exploited for halide perovskite epitaxy to overcome many of the epitaxial growth challenges outlined above and provide an ideal range of lattice constants (5.4-6.6 Å) closely matched to those of the halide perovskites (5.5-6.2 Å), with suitable wettability, and congruent ionic bonding. Moreover, metal halide salts are also low cost, require little wafer processing prior to epitaxial growth, can support epitaxial growth at room temperature to eliminate the impact of thermal expansion mismatch[25], and can be wet-etched for epitaxial lift-off for a range of applications. In this work we focus on $CsSnBr_3$ as it has been shown to be a promising and air-stable candidate in optoelectronics[11] with a bandgap of 1.8 eV, but find this approach to be generally applicable across the halide (X) series. The lattice constant of cubic $CsSnBr_3$ (5.80 Å, see **Figure S1**) is most closely lattice matched from all the MX alkali halide salts with NaCl (cubic lattice constant of 5.64 Å). While the compressive misfit between $CsSnBr_3$ and NaCl is -2.8%, this provides one of the smallest misfits readily available.

Thin film cesium tin bromide was grown epitaxially on NaCl single crystalline substrates via reactive thermal deposition of CsBr and $SnBr_2$. The crystal growth was monitored *in situ* and in real-time with ultra-low current reflection high-energy electron diffraction (RHEED)[25] that enables continuous monitoring even on insulating substrates. RHEED patterns captured during the epitaxial growth of the perovskite at room temperature are shown in **Figure 1**. The first row of **Figure 1A** shows the initial RHEED patterns of the NaCl(100) crystal with the electron beam directed along the NaCl[110]. The impact of the precursor ratio on the crystal structure of epitaxial film is investigated with CsBr:$SnBr_2$ molar ratios ranging from 0.25:1 to 1.5:1. As a control experiment, the individual

growths of both precursors CsBr and $SnBr_2$ on NaCl(100) surface show distinct (and rotationally-disordered) patterns from the reacted perovskite film (shown in **Figure S2)**. We also confirm that the epitaxially deposited halide perovskite films form single-domain epitaxial layers from the rotation dependent RHEED (**Figure S3A-D**) and are strongly bonded to the metal halide crystals (see **Figure S4A-C**). The strong bond formed at the interface of the halide perovskite and metal halide substrates is very likely due to the similar ionic characteristic between halide perovskite and metal halide salt. This is confirmed by the attempted growth of halide perovskite on Ge and InP substrates, which have similar degree of lattice misfit but are more covalent in their bonding character. According to the RHEED pattern shown in **Figure S5**, neither Ge nor InP provides readily suitable surfaces for epitaxial growth of halide perovskite, which leads to the formation of polycrystalline films.

With the successful growth of single-domain epitaxial films we further demonstrate an epitaxial lift-off (ELO) process to allow the separation of these epitaxial layers from single crystalline substrates and enable substrate regrowth (see **Figure S6A and B-D** respectively). ELO has been shown to be an important processing method for making, for example, single-domain GaAs more economically viable for solar cells.[30] In our work this is achieved by flash cooling/heating with liquid nitrogen immersion followed by rapid immersion in diethyl ether to initiate cracking at the interface of the substrate and epitaxial film by differences in the thermal expansion coefficients. Subsequently, epitaxial films are peeled with conductive copper tape. Moreover, the substrates can be reused for further epitaxial growth (**Figure S6B-D**).

When depositing $CsSnBr_3$ using a molar ratio of 1:1 ($CsBr:SnBr_2$), the RHEED patterns remain streaky, indicating the formation of a smooth crystalline layer. After the deposition of the first monolayer, the underlying substrate Kikuchi lines disappear as expected due to the shift in

elemental composition and lattice type (face-centered to primitive). The geometry and spacing of these reciprocal lattice points obtained along the [110] and [100] direction indicate that the crystal structure of the perovskite is cubic with a calculated lattice constant of 5.8±0.1 Å (shown in Figure S3A-D). The lattice constant is further confirmed with *ex situ* X-ray diffraction (XRD) to obtain an out-of-plane lattice constant of 5.80±0.01 Å (discussed below). Several other bulk phases have been reported for $CsSnBr_3$, including tetragonal and monoclinic phases; however, only the cubic phase is stable at room temperature[31, 32]. The high symmetry shown in all of the diffraction data clearly indicate the presence of the cubic phase (Figure 3SA-D). Thus, we find the films are not pseudomorphic past the first monolayer, which is not surprising considering the level of compressive misfit. This implies there is a small critical thickness and that there will be a considerable dislocation density to accommodate this misfit. However, because it is compressive misfit, this is less likely to lead to film cracking than if it were tensile misfit,[33] and no cracking is observed for thicknesses > 2000 Å. During the 1:1 growth, we also observe clear RHEED oscillations that vary with deposition rate. Such oscillations are a hallmark of layer-by-layer growth (**Figure S7**), where the oscillation period typically corresponds to the growth of a monolayer or bilayer,[34] but can also show complex bimodal periods.[35] Here, we find the oscillation period corresponds to half a monolayer (two periods per monolayer), which suggests a more complex underlying reactive growth mechanism or an associated reconstruction during the reaction. This is also similar to RHEED oscillation beating seen in ZnSe migration-enhanced epitaxial growth on GaAs where the oscillation period corresponded to a half monolayer.[36] Cross-section TEM images of the epitaxial $CsSnBr_3$ film are shown in **Figure 2**. Due to the inherent misfit, we do observe dislocations in the first several monolayers at the interface (see **Figure S8B**) when no pseudomorphic layer is present. Nonetheless,

the atomic arrangement of the two materials are nearly indistinguishable, which is consistent with the observation of the RHEED patterns. The cross-section and top-view SEM images respectively shown in **Figure 2C** and **Figure S9** further confirms the smooth surface of films prepared with 1:1 ratio of CsBr and $SnBr_2$, indicating its suitability for the fabrication of thin-film optoelectronic devices.

In contrast to the growth with a 1:1 stoichiometry, growth with a 0.5:1 stoichiometry results in a phase transition from the cubic $CsSnBr_3$ to a stable tetragonal phase that takes place at the earliest stages of growth within the first two monolayers. Rotation dependent RHEED patterns for the tetragonal phase are shown in **Figure S3E-H**. While tetragonal distortions are common for large lattice misfits in pseudomorphic growth, this tetragonal phase is not a simple distortion, nor is it the low temperature tetragonal phase reported in Ref[31, 32]; it even appears to be a monoclinic phase when monitored along the NaCl [110] direction. Upon closer inspection of the RHEED data, simulated selected area electron diffraction (SAED) patterns of the new phase is identified as the $CsSn_2Br_5$ phase (see **Figure S10** and detailed discussion in Supporting Information). This indicates that the growth with moderate Cs deficiency leads to a susceptibility to transitioning to $CsSn_2Br_5$. This phase transition process is further elucidated by the RHEED data in **Figure S11** where only the first ML is cubic and then the subsequent layers transform to the tetragonal phase. Real time RHEED videos showing the phase transition are available in the Supporting Information (**Movie S1**). The transition was monitored under rough growth conditions with substrates fixed at NaCl [110] due to the symmetry and lattice matching of the *a-b* plane of the tetragonal phase. The RHEED intensity monitoring also allows the study of phase transitions from cubic to tetragonal because RHEED pattern changes can be monitored as a change of particular diffraction peak locations (**Figure S12)**.

At later stages of growth (>7 MLs) the spotty patterns of the tetragonal phase become streaky, which is indicative of the crystalline film changing from rough to smooth while maintaining the initial tetragonal crystal structure.

To further confirm the phases shown in the RHEED patterns, XRD was used to determine the out-of-plane lattice parameter for the epitaxial films. As the ratio of CsBr to $SnBr_2$ increases from 0.25:1 to 1:1, the peaks at 11.57° (*d* = 7.64±0.01 Å) and 23.46° are replaced by peaks at 15.31° (*d* = 5.80±0.01 Å) and 30.83° as shown in **Figure S13**. The observed peaks are consistent with the *d*-spacings along the *c*-axis calculated from RHEED patterns and correspond to the (001)/(002) and (002)/(004) peaks of the cubic $CsSnBr_3$ and tetragonal $CsSn_2Br_5$ phases respectively. Based on the RHEED and XRD data, the measured lattice constants and orientations of the two epitaxial phases are summarized in **Table S1**, along with simulated XRD patterns of polycrystalline $CsSnBr_3$ and $CsSn_2Br_5$ (**Figure S14)**. Surprisingly, we find that both the cubic $CsSnBr_3$ and tetragonal $CsSn_2Br_5$ can grow epitaxially, even though the lattice constant of $CsSn_2Br_5$ is much larger and the mismatch between $CsSn_2Br_5$ and NaCl is 4.9 %. This larger lattice is accommodated via the rotation of $CsSn_2Br_5$ relative to the metal halide substrate. Schematics of the epitaxial growth of $CsSn_2Br_5$ and $CsSnBr_3$ on NaCl substrates are shown in **Figure 2**.

Epitaxial growths with both a greater CsBr deficiency (0.25:1) and CsBr excess (1.5:1) were also investigated as shown in **Figure 1**. At the CsBr deficient (0.25:1) ratio, the pure tetragonal phase is observed without first seeing the cubic structure. In contrast, the CsBr excess (1.5:1) ratio resulted in ring-like patterns, which indicates the film becomes a three-dimensional polycrystalline powder which is consistent with the XRD pattern shown in **Figure S15**.

Epitaxial films were also characterized by X-ray photoelectron spectroscopy (XPS) as shown in **Figure S16-17** to measure the elemental ratios in the films deposited using various ratios. By fitting the XPS peak, the elemental ratio of Cs to Sn can be extracted, and the results are summarized in **Table S2-3**. The epitaxial film deposited with 1:1 ratio of CsBr to $SnBr_2$ is indeed stoichiometric $CsSnBr_3$ (1:1:3 for Cs:Sn:Br). The other two ratios of 0.25:1 and 0.5:1 both lead to films deficient in Cs. The combination of RHEED, XRD and XPS analysis indicates that the growth of $CsSnBr_3$ is more favorable when Cs is stoichiometric or in slight excess, while $CsSn_2Br_5$ dominates when there is a Cs deficiency.

Both selective elemental vacancies and lattice misfit can ultimately play a role in initiating strain-driven phase transitions in these systems. While the elemental vacancies can be controlled by stoichiometry, the lattice misfit can be tuned through compositional alloying of the metal halide substrate, either in the bulk or as thin pseudomorphic interlayers. NaBr has larger lattice constant (5.98 Å) than cubic $CsSnBr_3$. Therefore, we demonstrate that alloying NaBr and NaCl can provide near perfect lattice matching for epitaxial growth of cubic $CsSnBr_3$ (**Figure S18-S19**), representing a general strategy for tuning the lattice misfit and dislocation density.

Experimental and theoretical studies are performed on the $CsSn_2Br_5$ and $CsSnBr_3$ phases to understand the properties for each. Absorption spectra of as-prepared epitaxial films are shown in **Figure S20** and confirm that the band-gap of epitaxial $CsSnBr_3$ is 1.83±0.02 eV, which is consistent with both theoretical[37] and experimental[31] results reported previously. For $CsSn_2Br_5$, we measure a bandgap of 3.34±0.04 eV, which is clearly distinguishable from the NaCl bandgap of ~9 eV (see **Figure S20B**). The calculated band structures, density of states (DOS) and projected density of states (PDOS) of $CsSnBr_3$ and $CsSn_2Br_5$ using the DFT with the HSE06 functional (see methods section) are

shown in **Figure 3C-D**. A summary of the calculated band gap values can be found in **Table S4**. The resulting HSE06 band gaps for $CsSnBr_3$ and $CsSn_2Br_5$ are 0.84 eV and 3.12eV, respectively. Note that DFT methods underestimate the gap of most semiconductors. These values are in reasonable agreement with the observed properties of $CsSnBr_3$ and $CsSn_2Br_5$. Had the perovskite been pseudomorphic on pure NaCl, we predict that the bandgap would decrease by around 0.5 eV (see **Figure S21**), which is clearly not observed experimentally. For comparison, the PBE band structures, DOS and PDOS of $CsSnBr_3$ and $CsSn_2Br_5$ are shown in **Figure S22**. These calculations further confirm that the tetragonal phase is $CsSn_2Br_5$ with a large bandgap.

Given the suitable bandgap of $CsSnBr_3$ for solar cell applications we fabricate photovoltaic devices to compare the optoelectronic properties of single-domain epitaxial films and amorphous films of $CsSnBr_3$. AFM images show that the surface of epitaxial films are much smoother than that of amorphous films (see **Figure S23A-B**). Current-voltage (*I-V)* curves measured by conducting probe AFM show that the devices fabricated with the single-domain epitaxial film as the absorber layers have both higher $I_{sc}$ and $V_{oc}$ than the control devices fabricated with amorphous films by a factor of 10 and 2 respectively (see **Figure S23C-D**). This clearly indicates that the high defect concentration present in amorphous and polycrystalline $CsSnBr_3$ is indeed a key limitation for enhancing device performance[11] that can be overcome with epitaxial layers.

Based on the control afforded by this epitaxial halide growth, we further fabricate quantum wells with varying well thicknesses for $CsSnBr_3$ paired with both vapor-deposited NaCl and $CsSn_2Br_5$ as the well barrier. Quantum wells are important in a range of optoelectronic devices and provide critical insight into the physical properties of quantum confined charge carriers, two-dimensional electron gas,[38] and tunable luminescence. The growth process was investigated by RHEED to

confirm the formation of epitaxial multilayers as shown in **Figure 4A-C** (and **Figure S24** for a greater number of layers**)** where NaCl was grown under similar conditions to homoepitaxial growth demonstrated previously.[25] The data in Figure 4 shows that no obvious change occurs after depositing the epitaxial barrier layer on the halide perovskite or after depositing multiple quantum well layers. That is, the NaCl epitaxial layers are pseudomorphic with the perovskite film. The PL spectrum of $CsSnBr_3$/NaCl quantum wells were studied by adjusting the well thickness shown schematically in **Figure 4D**. When the well thickness is reduced from 100 nm to 5 nm, the emission peak redshifts (**Figure 4E**) to a similar degree as seen with colloidal nanocrystals.[39] From fitting the size dependence of the bandgap, we can estimate an effective reduced mass of $m^* = 0.30\ m_e$, where $m_e$ is the rest mass of the electron, and the Bohr radius of $CsSnBr_3$ of ~5.6 nm (see fitting discussion in Supplementary Text). This is similar in magnitude to CdSe (5.6 nm)[40] and Si (~5nm)[41], smaller than PbS (20 nm)[42] and larger than ZnS (2.5 nm).[43] In moving from the weak to strong confinement regime, we expect that the bandgap of $CsSnBr_3$ to reach up to 3.0 eV with the smallest well thickness around 1 nm. We note that quantum wells with $CsSn_2Br_5$ barrier layers were also feasible through switching of the stoichiometry. As shown in **Figure S25** and **Table S6**, the PL spectra of $CsSnBr_3$/$CsSn_2Br_5$ quantum wells show consistent changes with those of $CsSnBr_3$/NaCl quantum wells when varying well thickness. This provides a route to better index-match the two layers in multiple quantum wells with enhanced potential for electrical injection.

In summary, we demonstrate a route to the room-temperature epitaxial growth of inorganic halide perovskites using low cost metal halide crystals and show the emergence of two epitaxial phases of cesium tin bromide ($CsSnBr_3$ and $CsSn_2Br_5$) with vastly differing lattice constants and bandgaps based on stoichiometry control. The larger lattice of $CsSn_2Br_5$ is accommodated via the

rotation of crystal planes relative to the metal halide substrates. The phase transitions between the cubic $CsSnBr_3$ and tetragonal $CsSn_2Br_5$ phases were manipulated and observed in real-time. The lattice misfit between the ionic epitaxial film and the substrate is precisely tuned by applying a pseudomorphic buffer layer of alloyed alkali metal halide salts and an epitaxial lift-off method has been demonstrated for further device fabrication. The dominant performance of devices fabricated with the epitaxial film confirms that the high crystallinity and low defect intensity are beneficial for halide perovskite optoelectronic applications. We further exploit the epitaxial growth of $CsSnBr_3$ to demonstrate multilayer epitaxial quantum wells of a halide perovskite and extract the Bohr radius for $CsSnBr_3$ of 5.6 nm, which provides a guide for manipulating quantum confinement in this class of materials. These demonstrations could spark the exploration of a full range of epitaxial halide perovskites and help enable their ultimate potential in many emerging applications.

**4. Experimental Section**

*Epitaxial Film and Quantum Well Growth:* Reactive vapor deposition of halide perovskites was performed in a multisource custom thermal evaporator (Angstrom Engineering) equipped with reflection high energy electron diffraction (RHEED) system (STAIB Instruments). The two precursors, CsBr and $SnBr_2$, were co-evaporated from separate tungsten boats to form the perovskite layer. Prior to growth, pre-polished NaCl (100) single crystal substrates were prepared through cleaving in a glovebox or used as polished. Epitaxial growth was performed under a base pressure less than $3\times10^{-6}$ torr and deposition rates were measured *in situ* with quartz crystal microbalances for each source. The crystal structure was monitored in real-time and *in situ* using RHEED (30.0 keV) optimized with an ultra-low current (< 10 nA) to eliminate damage and charging of the film over the growth times investigated. RHEED oscillations were monitored with substrates fixed at various in-plane orientations (KSA400). Rotation dependent RHEED patterns were collected after each deposition was halted via source and substrate shutters. Quantum well multilayers were fabricated

under similar growth conditions, where epitaxial NaCl was vapor deposited from a NaCl powder source with a rate of 0.02 Å/s and a thickness of 1.5 nm.

*Epitaxy Lift-Off and Device Fabrication:* Epitaxial lift off was performed by immersing the epitaxial film grown on the substrate into liquid nitrogen for about 30 s. The film and substrate were then quickly immersed into diethyl ether. After warming to room temperature, the film and substrate were removed from the solvent and copper tape was pressed onto the halide perovskite film (with a pre-deposited gold layer of ~300 Å on top). The tape was slowly peeled to separate the halide perovskite epitaxial film from the substrate. $C_{60}$ (M. E. R. Corporation 99.9%), bathocuproine (BCP, Lumtec >99%), silver (Kurt Lesker, 99.99%), and tris-(8-hydroxyquinolinato) aluminum ($Alq_3$, Lumtec, >99.5%) were then deposited onto the surface of halide perovskite film in sequence followed by Ag(4nm)/$Alq_3$(60nm) as the transparent cathode for top illumination.

*Material Characterization:* Cross-section transmission electron microscope (TEM) samples were prepared by focused ion beam (FIB), attached to a FEI Nova 200 Nanolab SEM/FIB, and then investigated by a JEOL 3100R05 Double Cs Corrected TEM/STEM. A carbon top-layer was deposited on the cutting area to protect the epitaxial film. Scanning electron microscopy (SEM, Carl Zeiss Auriga Dual Column FIB SEM) was performed for *ex situ* film thickness calibration and morphology characterization. Photoluminescence spectra were measured using a PTI Quanta Master 40 spectroflurometer under nitrogen atmosphere and various excitation wavelengths. Dielectric long-pass filters were used during the PL measurement to prevent both wavelength doubling and light bleeding. UV-VIS transmission spectra were taken using Perkin Elmer UV-VIS Spectrometer (Lambda 900). X-ray diffraction was characterized by using a Bruker D2 Phaser XRD instrument with a Cu Kα source at 30 kV and 10 mA and a Ni filter in the Bragg-Brentano configuration. X-ray photoelectron spectroscopy was performed in a separate chamber with a Kratos Axis Ultra XPS using a monochromated AlKα (1.486 keV) as the X-ray source. Before collecting XPS data, the films were etched by Argon ions for 1.5 min to prevent the interference of surface contamination.

*Device Characterization:* photoconductive-atomic force microscope (AFM) measurements were carried out on a MFP-3D-AFM from Asylum Research in a nitrogen filled cell. The illumination condition was established by a light fiber shining from the top of the sample. Pt/Ir coated tip with

the spring constant of 0.2 N/m was used in the pc-AFM measurements, while 20 nN force was applied between tip and sample. As the tip moved across the surface, the topology was measured. In the point *I-V* measurements, the AFM tip was fixed at different locations. While a bias connected to the bottom electrode was varied, the current between the AFM tip and bottom electrode was recorded.

*Calculation of Crystal and Band Structures:* Electronic band structures and densities of states (DOS) of $CsSnBr_3$ and $CsSn_2Br_5$ were calculated using density functional theory (DFT) implemented in the Vienna Ab initio Simulation Package (VASP). The exchange-correlation functional utilized were the Perdew-Burke-Ernzerhof (PBE) functional[44], which belongs to the generalized gradient approximations (GGA) class, and the screened Heyd-Scuseria-Ernzerhof (HSE06)[45] hybrid functional. Additional computational details can be found in the Supporting Information. Crystal structures were drawn using VESTA and SAED patterns were calculated with CrystalMaker.

**Supporting Information**

Supporting Information is available from the Wiley Online Library or from the author.

**Acknowledgements**

The work at Michigan State University was supported by the Camille and Henry Dreyfus Postdoctoral Program in Environmental Chemistry (material synthesis and growth), the U.S. Department of Energy (DOE) Office of Science, Basic Energy Sciences (BES), under Award # DE-SC0010472 (structural characterization), and a Michigan State University Strategic Partnership Grant (SPG) (optical characterization). The FEI Nova 200 Nanolab SEM/FIB and the JEOL-JEM 3100R05 Double Cs-corrected TEM/STEM were under the support of the University of Michigan College of Engineering and NSF grant #DMR-0320740 and NSF grant #DMR-0723032, respectively.

The authors thank Dr. Benjamin G. Levine and Dr. Per Askeland for their helpful discussions on quantum confinement and material characterization, respectively.

Received: ((will be filled in by the editorial staff))
Revised: ((will be filled in by the editorial staff))
Published online: ((will be filled in by the editorial staff))



**References and Notes:**

[1] a) W. Nie, H. Tsai, R. Asadpour, J.-C. Blancon, A. J. Neukirch, G. Gupta, J. J. Crochet, M. Chhowalla, S. Tretiak, M. A. Alam, H.-L. Wang, A. D. Mohite, *Science* 2015, **347**, 522; b) F. Wang, H. Yu, H. Xu, N. Zhao, *Advanced Functional Materials* 2015, **25**, 1120; c) S. Kazim, M. K. Nazeeruddin, M. Grätzel, S. Ahmad, *Angewandte Chemie International Edition* 2014, **53**, 2812.

[2] X. Gong, Z. Yang, G. Walters, R. Comin, Z. Ning, E. Beauregard, V. Adinolfi, O. Voznyy, E. H. Sargent, *Nature Photonics* 2016, **10**, 253.

[3] G. Xing, N. Mathews, S. S. Lim, N. Yantara, X. Liu, D. Sabba, M. Grätzel, S. Mhaisalkar, T. C. Sum, *Nature Materials* 2014, **13**, 476.

[4] A. Swarnkar, A. R. Marshall, E. M. Sanehira, B. D. Chernomordik, D. T. Moore, J. A. Christians, T. Chakrabarti, J. M. Luther, *Science* 2016, **354**, 92.

[5] J. Luo, J. H. Im, M. T. Mayer, M. Schreier, M. K. Nazeeruddin, N.-G. Park, S. D. Tilley, H. J. Fan, M. Grätzel, *Science* 2014, **345**, 1593.

[6] Y. Fang, Q. Dong, Y. Shao, Y. Yuan, J. Huang, *Nature Photonics* 2015, **9**, 679.

[7] http://www.nrel.gov/ncpv/images/efficiency_chart.jpg.

[8] a) I. R. Benmessaoud, A.-L. Mahul-Mellier, E. Horvath, B. Maco, M. Spina, H. A. Lashuel, L. Forro, *Toxicology Research* 2016, **5**, 407; b) A. Babayigit, A. Ethirajan, M. Muller, B. Conings, *Nature Materials* 2016, **15**, 247.

[9] M. Grätzel, *Nature Materials* 2014, **13**, 838.

[10] a) T.-B. Song, T. Yokoyama, S. Aramaki, M. G. Kanatzidis, *ACS Energy Letters* 2017, **2**, 897; b) T.-B. Song, T. Yokoyama, C. C. Stoumpos, J. Logsdon, D. H. Cao, M. R. Wasielewski, S. Aramaki, M. G. Kanatzidis, *Journal of the American Chemical Society* 2017, **139**, 836.

[11] D. Moghe, L. Wang, C. J. Traverse, A. Redoute, M. Sponseller, P. R. Brown, V. Bulović, R. R. Lunt, *Nano Energy* 2016, **28**, 469.

[12] E. A. Schiff, *Solar Energy Materials and Solar Cells* 2003, **78**, 567.

[13] T. Kamiya, H. Hosono, *NPG Asia Materials* 2010, **2**, 15.

[14] D. Jurbergs, E. Rogojina, L. Mangolini, U. Kortshagen, *Applied Physics Letters* 2006, **88**, 233116.

[15] a) Q. Dong, Y. Fang, Y. Shao, P. Mulligan, J. Qiu, L. Cao, J. Huang, *Science* 2015, **347**, 967; Y. Liu, Z. Yang, D. Cui, X. Ren, J. Sun, X. Liu, J. Zhang, Q. Wei, H. Fan, F. Yu, *Advanced Materials* 2015, **27**,

5176; b) M. I. Saidaminov, A. L. Abdelhady, B. Murali, E. Alarousu, V. M. Burlakov, W. Peng, I. Dursun, L. Wang, Y. He, G. Maculan, *Nature communications* 2015, **6**; c) D. Shi, V. Adinolfi, R. Comin, M. Yuan, E. Alarousu, A. Buin, Y. Chen, S. Hoogland, A. Rothenberger, K. Katsiev, *Science* 2015, **347**, 519; d) Y. Dang, Y. Zhou, X. Liu, D. Ju, S. Xia, H. Xia, X. Tao, *Angewandte Chemie* 2016, **128**, 3508.

[16] A. F. Santander-Syro, O. Copie, T. Kondo, F. Fortuna, S. Pailhes, R. Weht, X. G. Qiu, F. Bertran, A. Nicolaou, A. Taleb-Ibrahimi, P. Le Fevre, G. Herranz, M. Bibes, N. Reyren, Y. Apertet, P. Lecoeur, A. Barthelemy, M. J. Rozenberg, *Nature* 2011, **469**, 5.

[17] H. Y. Hwang, Y. Iwasa, M. Kawasaki, B. Keimer, N. Nagaosa, Y. Tokura, *Nature Materials* 2012, **11**, 103.

[18] T. Pešić-Brđanin, B. L. Dokić, *Electronics* 2014, **18**, 63.

[19] J. A. Mundy, C. M. Brooks, M. E. Holtz, J. A. Moyer, H. Das, A. F. Rébola, J. T. Heron, J. D. Clarkson, S. M. Disseler, Z. Liu, Nature 2016, 537, 523.

[20] A. Tsukazaki, S. Akasaka, K. Nakahara, Y. Ohno, H. Ohno, D. Maryenko, A. Ohtomo, M. Kawasaki, *Nature materials* 2010, **9**, 11.

[21] L. Yao, S. Inkinen, S. van Dijken, *Nature Communications* 2017, **8**, 14544.

[22] a) H. Sun, W. Tian, X. Pan, J. H. Haeni, D. G. Schlom, *Applied Physics Letters* 2004, **84**, 3298; b) D. G. Schlom, L.-Q. Chen, C. J. Fennie, V. Gopalan, D. A. Muller, X. Pan, R. Ramesh, R. Uecker, *MRS Bulletin* 2014, **39**, 118.

[23] J. Mannhart, D. G. Schlom, *Science* 2010, **327**, 1607.

[24] A. A. Demkov, A. B. Posadas, *Integration of functional oxides with semiconductors*, Springer Science & Business Media, 2014.

[25] P. Chen, P. S. Kuttipillai, L. Wang, R. R. Lunt, *Sci Rep* 2017, **7**, 40542.

[26] Y. Wang, Y. Shi, G. Xin, J. Lian, J. Shi, *Crystal Growth & Design* 2015, **15**, 4741.

[27] Y. Wang, Z. Chen, F. Deschler, X. Sun, T.-M. Lu, E. A. Wertz, J.-M. Hu, J. Shi, *ACS Nano* 2017, **11**, 3355.

[28] J. Chen, Y. Fu, L. Samad, L. Dang, Y. Zhao, S. Shen, L. Guo, S. Jin, *Nano Letters* 2017, **17**, 460.

[29] a) S. T. Ha, X. Liu, Q. Zhang, D. Giovanni, T. C. Sum, Q. Xiong, *Advanced Optical Materials* 2014, **2**, 838; b) M. Sytnyk, S. Yakunin, W. Schöfberger, R. T. Lechner, M. Burian, L. Ludescher, N. A. Killilea, A. YousefiAmin, D. Kriegner, J. Stangl, H. Groiss, W. Heiss, *ACS Nano* 2017, **11**, 1246.

[30] a) H. Taguchi, T. Soga, T. Jimbo, *Solar Energy Materials and Solar Ccells* 2005, **85**, 85; b) C.-W. Cheng, K.-T. Shiu, N. Li, S.-J. Han, L. Shi, D. K. Sadana, *Nature communications* 2013, **4**, 1577; c) W. Choi, C. Z. Kim, C. S. Kim, W. Heo, T. Joo, S. Y. Ryu, H. Kim, H. Kim, H. K. Kang, S. Jo, *Advanced Energy Materials* 2014, **4**; d) F.-L. Wu, S.-L. Ou, R.-H. Horng, Y.-C. Kao, *Solar Energy Materials and Solar Cells* 2014, **122**, 233.

[31] S. J. Clark, C. D. Flint, J. D. Donaldson, *Journal of Physics and Chemistry of Solids* 1981, **42**, 133.

[32] M. Mori, H. Saito, *Journal of Physics C: Solid State Physics* 1986, **19**, 2391.

[33] U. W. Pohl, *Epitaxy of semiconductors: introduction to physical principles*, Springer Science & Business Media, 2013.

[34] M. Müller, *Electronic Structure of Ferromagnet Insulator Interfaces: Fe/MgO and Co/MgO*, Vol. 40, Forschungszentrum Jülich, 2007.
[35] C. L. Berrie, S. R. Leone, *Journal of Crystal Growth* 2000, **216**, 159.
[36] J. M. Gaines, C. A. Ponzoni, *Surface Science* 1993, **290**, 172.
[37] L.-Y. Huang, W. R. Lambrecht, *Physical Review B* 2013, **88**, 165203.
[38] A. J. Garza, G. E. Scuseria, *The Journal of Physical Chemistry Letters* 2016, **7**, 4165.
[39] T. C. Jellicoe, J. M. Richter, H. F. Glass, M. Tabachnyk, R. Brady, S. E. Dutton, A. Rao, R. H. Friend, D. Credgington, N. C. Greenham, *Journal of the American Chemical Society* 2016, **138**, 2941.
[40] R. W. Meulenberg, J. R. I. Lee, A. Wolcott, J. Z. Zhang, L. J. Terminello, T. van Buuren, *ACS Nano* 2009, **3**, 325.
[41] M. R. Bergren, P. K. B. Palomaki, N. R. Neale, T. E. Furtak, M. C. Beard, *ACS Nano* 2016, **10**, 2316.
[42] F. W. Wise, *Accounts of Chemical Research* 2000, **33**, 773.
[43] B. Bhattacharjee, D. Ganguli, K. Iakoubovskli, A. Stesmans, S. Chaudhuri, *Bulletin of Materials Science* 2002, **25**, 175.
[44] J. P. Perdew, K. Burke, M. Ernzerhof, *Physical Review Letters* 1996, **77**, 3865.
[45] J. Heyd, G. E. Scuseria, M. Ernzerhof, *The Journal of Chemical Physics* 2003, **118**, 8207.

**Figures**

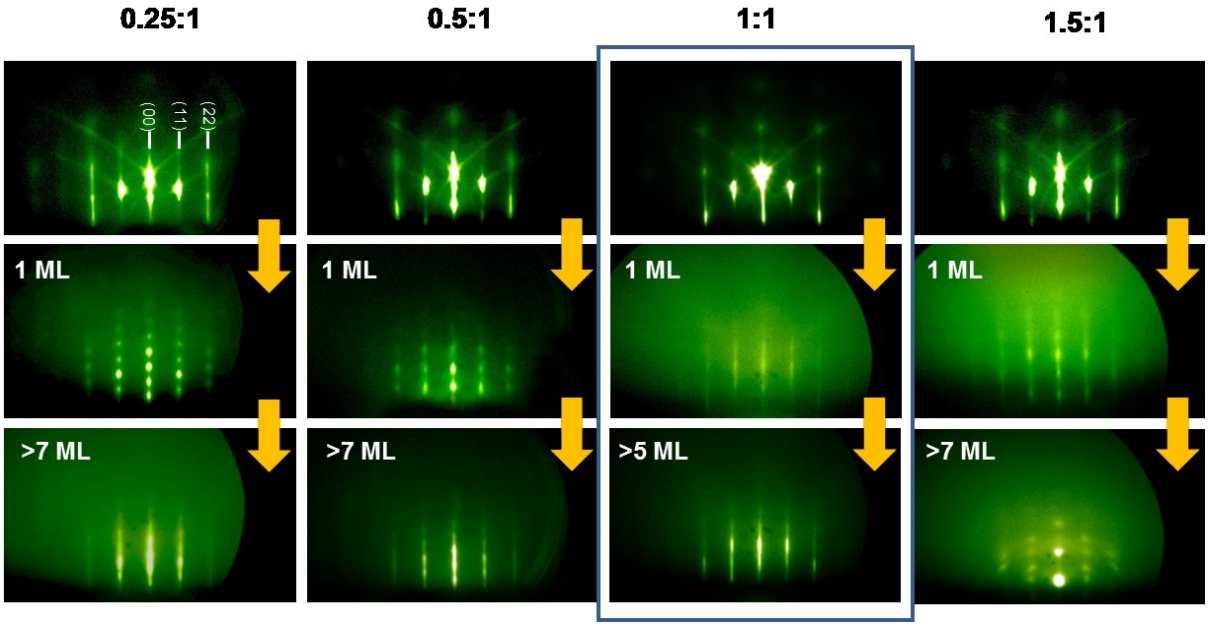


**Figure 1. In situ RHEED patterns of the epitaxial growth of $CsSnBr_3$.** The epitaxial halide perovskite film is grown on single crystalline NaCl(100) substrates with various ratios of precursors, CsBr to $SnBr_2$, where two distinct phases are observed depending on stoichiometry: cubic (1:1) and tetragonal (0.25:1 and 0.5:1). The epitaxial growth of stoichiometric $CsSnBr_3$ (cubic) is highlighted in the box. The uncertainty of film thickness is 1-1.5 MLs.

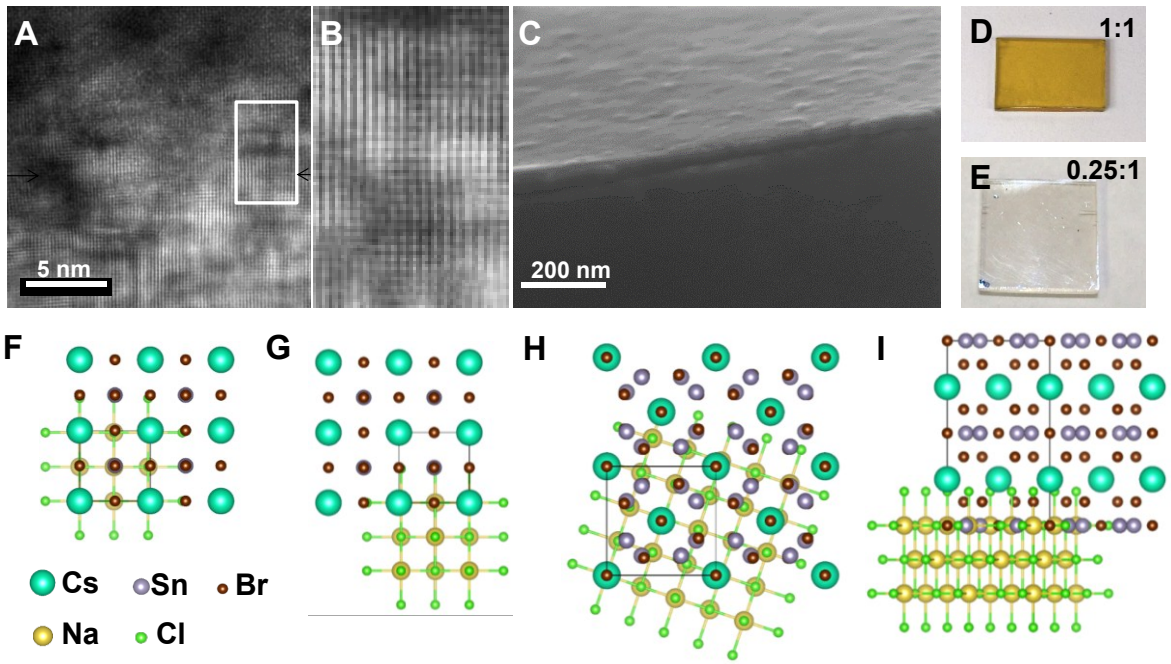


**Figure 2. Ordering of the halide perovskite at the halide salt interface.** (A) Enlarged cross-section TEM image (viewed along the [100] direction of NaCl) of sample prepared at 1:1 CsBr:$SnBr_2$ ratio with $CsSnBr_3$ film thickness of ~25 nm, where the black arrow shows the boundary between epitaxy and NaCl. The original image is shown in fig. S6; (B) Enlarged image of the area marked by white frame; (C) cross-section SEM image showing the smooth surface of epitaxial film. (D) and (E) show the film color prepared at different ratios 0.25:1 and 1:1, respectively. Schematics of the epitaxial structures: (F) Top and (G) side view of cubic $CsSnBr_3$ on NaCl. (H) Top and (I) side view of tetragonal $CsSn_2Br_5$ on

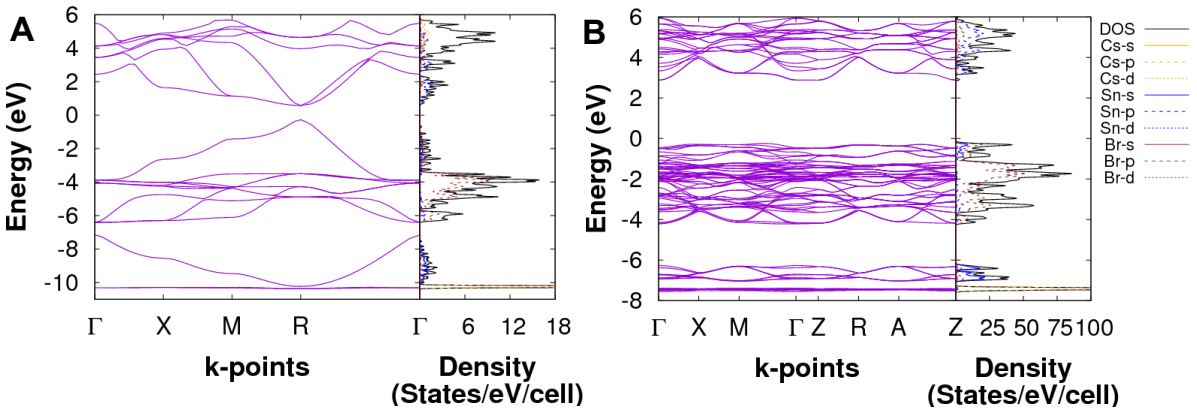


**Figure 3. Electronic band structures of two phases.** HSE06 band structure, density of states (DOS) and projected density of states (PDOS) of (A) $CsSnBr_3$ and (B) $CsSn_2Br_5$.

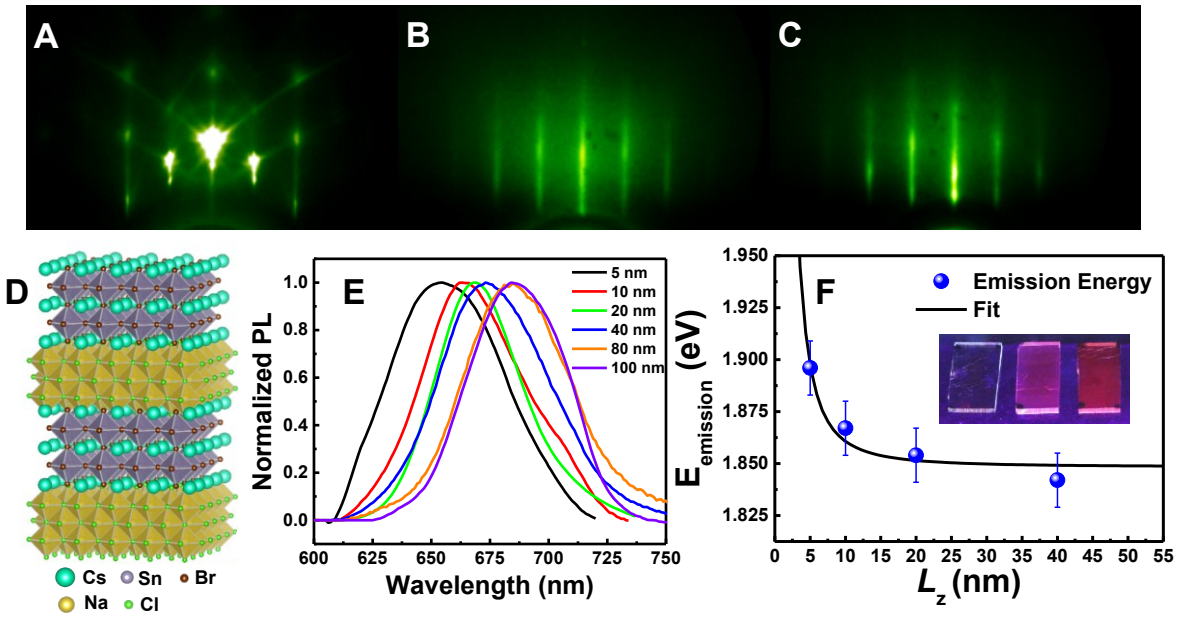


**Figure 4. 2D Quantum well fabrication.** RHEED patterns of (A) NaCl along the [110] direction, (B) NaCl/$CsSnBr_3$(~40 nm), and (C) NaCl/$CsSnBr_3$(~40 nm)/NaCl(1.5 nm). (D) Schematic illustration of NaCl/$CsSnBr_3$ quantum well structure, green spheres are Cs; gray spheres are Sn; red spheres are Br; yellow spheres are Na; and light green spheres are Cl; (E) PL spectra of quantum well samples with various well width: 5 nm (black curve), 10 nm (red curve), 20 nm (blue curve), 40 nm (magenta curve), 80 nm (orange curve), and 100 nm (violet curve). (F) Emission energy of quantum wells with varying well width. The fitting is described in the Supporting Information. The inset shows the photograph of samples illuminated under UV light. Samples from left to right are bare single crystal, quantum well of NaCl/$CsSnBr_3$(40 nm), and quantum well of NaCl/$CsSnBr_3$(~100 nm).

**Single-domain halide perovskite heteroepitaxy** has been demonstrated and multiple epitaxial phases of archtyptal halide perovskite have been uncovered via stiochiometry control. The epitaxial growth has been further exploited to demonstrate multilayer 2D quantum wells of a halide-perovskite system and could ultimately enable their full potential in many emerging applications.

*Keyword: halide perovskite; epitaxy; single-domain; 2D uantum well; vapor deposition*

*Dr. Lili Wang[a,†], Pei Chen[a,†], Dr. Non Thongprong[b], Margaret Young[a], Padmanaban S. Kuttipillai[a], Chuanpeng Jiang[b], Prof. Pengpeng Zhang[b], Dr. Kai Sun[c], Prof. Phillip M. Duxbury[b], Prof. Richard R. Lunt[a,b,*]*

***Unlocking the Single-Domain Epitaxy of Halide Perovskites***